Accepted Manuscript

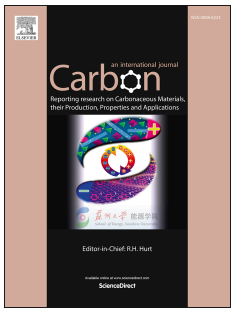

Carbon nanotube-supported Ni-CeO_2 catalysts. Effect of the support on the catalytic performance in the low-temperature WGS reaction

A.B. Dongil, L. Pastor-Pérez, N. Escalona, A. Sepúlveda-Escribano

PII: S0008-6223(16)30091-4

DOI: 10.1016/j.carbon.2016.01.103

Reference: CARBON 10723

To appear in: *Carbon*

Received Date: 7 July 2015

Revised Date: 22 January 2016

Accepted Date: 31 January 2016

Please cite this article as: A.B. Dongil, L. Pastor-Pérez, N. Escalona, A. Sepúlveda-Escribano, Carbon nanotube-supported Ni-CeO_2 catalysts. Effect of the support on the catalytic performance in the low-temperature WGS reaction, *Carbon* (2016), doi: 10.1016/j.carbon.2016.01.103.

Carbon nanotube-supported Ni-CeO_2 catalysts. Effect of the support on the catalytic performance in the low-temperature WGS reaction.

A.B. Dongil[1], L. Pastor-Pérez[2], N. Escalona[3,4], A. Sepúlveda-Escribano[*2]

[1] *Universidad de Concepción, departamento de físicoquímica, laboratorio de catálisis por metales, Edmundo Larenas 129, Concepción, Chile.*

[2] *Laboratorio de Materiales Avanzados, Departamento de Química Inorgánica - Instituto Universitario de Materiales de Alicante, Universidad de Alicante, Apartado 99, E-03080 Alicante, Spain.*

[3] *Departamento de Ingeniería Química y Bioprocesos, Escuela de Ingeniería, Pontificia Universidad Católica de Chile, Avenida Vicuña Mackenna 4860, Macul, Santiago, Chile.*

[4] *Facultad de Ciencias Químicas, Pontificia Universidad Católica de Chile.*

(*) Corresponding author. Tel: +34 965903974. E-mail: asepul@ua.es (A. Sepúlveda-Escribano)

Abstract

The low temperature water-gas shift (WGS) reaction has been studied over two commercial multiwall carbon nanotubes-supported nickel catalysts promoted by ceria. For comparison purposes, activated carbon-supported catalysts have also been studied. The catalytic performance and the characterization by N_2 adsorption analysis, powder X-ray diffraction (XRD), temperature-programmed reduction with H_2 (H_2-TPR), X-ray photoelectron spectroscopy (XPS) and transmission electron microscopy (TEM) analysis showed that the surface chemistry has an important effect on the dispersion of ceria. As a result, ceria was successfully dispersed over the carbon nanotubes (CNTs) with less graphitic character, and the catalyst afforded better activity in WGS than the catalyst prepared over massive ceria. Moreover, a 20 wt.% CeO_2 loading over this support was more active than the analogous catalyst with a 40 wt.% loading. The ceria nanoparticles were smaller when the support was previously oxidized, however this resulted in a decrease of the activity.

1. Introduction

Hydrogen is recognized as an ideal energy carrier, as it provides a high efficiency in power generation when it is used as a feed in fuel cells, being water the only by-product. However, hydrogen does not occur naturally and has to be produced, for example, by steam reforming of hydrocarbons derived from fossil fuels or of renewable feedstock [1]. The presence of small amounts of carbon monoxide (> 10 ppm) in the hydrogen stream may poison the platinum catalysts employed in the fuel cell electrodes. One of the alternatives to obtain a high purity hydrogen stream is to couple the reforming step with the water-gas shift reaction, WGS ($CO+H_2O \rightarrow CO_2+H_2$). The WGS reaction is slightly exothermic but, however, it is limited by kinetics at low temperature and thus it is carried out industrially in two stages. The first stage is performed at high temperatures (623-723 K) and the second one at low temperatures (453-573 K), with more active catalysts [2]. Several catalytic systems have been studied for this latter stage at low temperatures. Among them, ceria-supported metals (rhodium, platinum, palladium, nickel, iron, cobalt, and copper) are the most promising ones, and special attention has been paid to the platinum/ceria system [3,4]. Ceria, as a partially reducible oxide, may promote the mobility of surface oxygen species over the catalyst surface due to the $Ce^{+4} \leftrightarrow Ce^{+3}$ redox process [5]. Moreover, a synergy is obtained between the metal and ceria. On one hand, ceria reducibility is favored when the metal is in close contact with its surface and, on the other hand, ceria can stabilize the metal nanoparticles hindering their agglomeration [5,6]. However, given the low availability of ceria, it would be interesting to optimize its use by, for example, dispersing it onto a high surface area support. In this sense, we have previously reported the effect of ceria dispersed over Pt/activated carbon catalysts [7]. An optimal CeO_2-Pt interaction when the system is deposited on a high area support afforded better activity and allowed to

reduce the amount of ceria used. However, the extent of the surface area is not the only parameter to take into account, as it has been shown that carbon nanotubes, with less surface area than an activated carbon, yielded more active catalysts in supported Pt-CeO_2 systems for the preferential oxidation of CO in the presence of H_2 (PROX reaction) [8].

Another important issue when developing a catalyst for WGS is the replacement of platinum for an economically competitive metal which is also more resistant to deactivation, and nickel has proved to be active in WGS when it is highly dispersed [9, 10, 11]. In this sense, this work compares the catalytic behavior of Ni nanoparticles supported on two commercial carbon nanotubes (CNTs) and on an activated carbon (AC). The effects of the surface chemistry, morphology and ceria loading on the catalytic performance in the low temperature WGS reaction have been studied.

2. Experimental

2.1 Catalysts

Two different commercial carbon nanotubes and an activated carbon were used as starting materials: BAYTUBES C150 HP (Bayer Materials Science) CNTb, Nanocyl 3100 (95% purity) CNTn and activated carbon (AC) (RGC-30 from Mead Westvaco Ltd. A portion of the parent CNTb was oxidized in HNO_3 (65%) at 403 K for 24 h mL g^{-1} and labeled as CNTbox. For the impregnation with the cerium precursor, the corresponding amount of $Ce(NO_3)_3 \cdot 6H_2O$ (99.99%, Sigma–Aldrich) was dissolved in acetone. The parent CNTs were added to the solution, in a proportion of 10 mL g^{-1} of support, with stirring. After 12 h in a covered flask, the excess of solvent was slowly removed in a rotary evaporator under vacuum. The solid was finally dried in an oven for

24 h at 353 K and then heat treated during 5 h at 623 K under flowing Hr (50 mL min^{-1}), with a heating rate of 1 K min^{-1}, in order to slowly decompose the cerium nitrate to form CeO_2 and trying to avoid the modification of the carbon surface by the evolved nitrogen oxides. In this way, five samples were prepared which were denoted as CNTn/Ce20, CNTb/Ce20, CNTb/Ce40, CNTbox/Ce20 and AC/Ce20. The "20" and "40" refer to the wt.% ceria loading. Catalysts were prepared by using the proper amount of $Ni(NO_3)_2 \cdot 6H_2O$ (99.9 %, Sigma–Aldrich) dissolved in acetone to obtain 5 wt.% Ni, using 10 mL of solution per gram of solid. After stirring for 12 h, the solvent was removed under vacuum at 333 K. Finally, the materials were treated at 623 K for 5 h under flowing He (50 mL min^{-1}). According to this procedure, five catalysts were prepared which were labeled as Ni/CNTnCe20, Ni/CNTbCe20, Ni/CNTbCe40, Ni/CNTboxCe20 and Ni/ACCe20. For the sake of comparison, a 5 wt.% Ni catalyst was prepared over bulk ceria, Ni/CeO_2, as well as on the parent carbon supports, Ni/CNTn, Ni/CNTb, and Ni/AC.

2.2 Characterization

The actual ceria content of the supports was determined by burning off the carbon in air at 973 K and weighting the residue, using the parent carbon supports as a blank. Textural properties of the prepared materials were determined by nitrogen adsorption at 77 K on a Micromeritics ASAP 2010 apparatus. Before measurements, the samples were dried at 383 K for 12 h and out-gassed at 523 K under vacuum. The micropore volume, V_{micro}, was obtained by application of the Dubinin–Radushkevich (DR) equation to the adsorption isotherm. The volume of mesopores, V_{meso}, was estimated by subtracting the micropore volume from the uptake at a relative pressure of 0.95. The

surface area was calculated by application of the Brunauer-Emmett-Teller (B.E.T.) method.

Conventional transmission electron microscopy (TEM) analysis was carried out with a JOEL model JEM-210 electron microscope working at 200 kV and equipped with an INCA Energy TEM 100 analytical system and a SIS MegaView II camera. Samples for analysis were suspended in methanol and placed on copper grids with a holey-carbon film support.

Raman measurements were performed with a LabRam (Jobin-Ivon) micro-Raman spectrometer at 514 nm. The laser beam was focused onto the sample with a 100x objective. The laser intensity at the sample was kept below the threshold for any laser-induced changes in the Raman spectra and electrical transport characteristics.

X-ray powder diffraction patterns were recorded on a RigakuD/max-2500 diffractometer with Cu Kα radiation at 40 kV and 100 mA.

Temperature-programmed reduction (TPR) measurements were carried out in a U-shaped quartz cell using a 5% H_2/He gas flow of 25 cm^3 min^{-1} and about 0.15 g of sample, with a heating rate of 10 K min^{-1} (TPR/TPD2900 Micromeritics system). Hydrogen consumption was followed by on-line mass spectrometry (Pfeiffer, OmniStar GSD 301).

X-Ray photoelectron spectroscopy (XPS) analyses were performed with a VG-Microtech Multilab 3000 spectrometer equipped with a hemispherical electron analyzer and a Mg-Kα (h = 1253.6 eV; 1 eV = 1.6302·10-19 J) 300-W X-ray source. The powder samples were pressed into small Inox cylinders. The catalysts were reduced ex-situ (H_2, 623 K, 1 h) and then introduced in octane under inert atmosphere. Suspensions were evaporated in the XPS system under vacuum conditions. Before recording the spectra, the samples were maintained in the analysis chamber until a residual pressure of ca.

$5 \cdot 10-7$ N m^{-2} was reached. The spectra were collected at pass energy of 50 eV. The intensities were estimated by calculating the integral of each peak, after subtracting the S-shaped background, and by fitting the experimental curve to a combination of Lorentzian (30%) and Gaussian (70%) lines. The binding energy (BE) of the C l s peak of the support at 284.6 eV was taken as an internal standard. The accuracy of the BE values is ± 0.2 eV.

2.3 Water-gas shift reaction

The catalytic behavior of the prepared samples in the low temperature water–gas shift reaction was evaluated in a fixed bed flow reactor under atmospheric pressure at temperatures ranging from 413 K to 533 K. The molar composition of the feed gas stream was 1.87% CO, 35.92 % H_2O, and He balance, with a total flow of 100 mL min^{-1}. In addition, and trying to simulate a real outgas mixture from a reformer, experiments with a feed gas composed of 7 mol% CO, 30 mol% H_2O, 50 mol% H_2, and 9 mol% CO_2 in helium was tested. Activity studies were performed using 0.150 g of catalyst diluted with SiC, at a volume ratio of 1:1, to avoid thermal effects. Prior to the reaction, the catalysts were reduced under hydrogen during 1 h at 623 K. The composition of the gas stream exiting the reactor was determined by mass spectrometry (Pfeiffer, OmniStar GSD 301), and the catalytic activity will be expressed by the degree of CO conversion. Reaction at each temperature was stabilized for 1 h.

3. Results and discussion

3.1 Support characterization

The parent CNTs were characterized to assess for the differences in their morphology, textural properties and surface chemistry. The N_2 adsorption-desorption isotherms at 77 K on the CNTn and CNTb supports are reported in Fig. 1a. They both show the characteristic shape of mesoporous materials with an important increase of nitrogen adsorption at high relative pressure (0.8–0.9) and a well-defined hysteresis loop, which is related with inter-nanotube cavities. It has to be noted that the adsorbed amount at these high pressures is much larger for CNTn, and the hysteresis loop closes at a relative pressure of around 0.7. On the other hand, the hysteresis cycle for CNTb closes at a lower relative pressure, around 0.3. This indicates a much wider mesopore size distribution which can include the mesoporosity originated by the inner hollow cavity of open-ended CNTs [12].

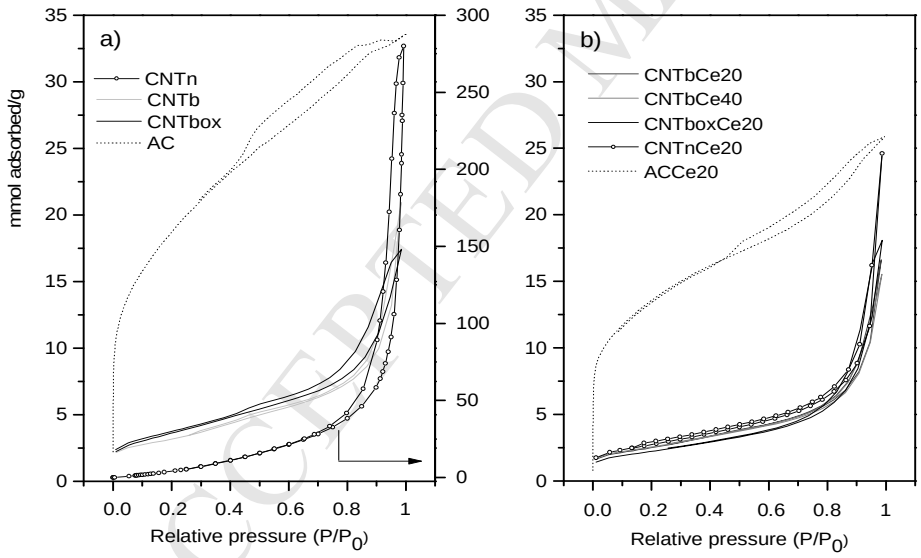

Figure 1. N_2 adsorption-desorption isotherms at 77 K.

Fig. 1a also includes the adsorption isotherm of AC, with a shape that corresponds to a combination of Type I and Type IV isotherms, characteristic of materials containing both micro- and mesopores. The estimated BET surface areas (Table 1) were 300 m^2 g^{-1} and 264 m^2 g^{-1} for CNTn and CNTb supports respectively, and 1487 m^2 g^{-1} for AC. As

the isotherms showed, the CNTn sample displayed a much larger proportion of mesopores than the CNTb and AC materials, which displayed a similar value. However, the microporous volume was much larger for this latter.

Table 1. Textural properties of the supports, and ceria content.

Sample	CeO_2(wt%)[1]	S_{BET}(m^2/g)	V_{micro}(cm^3/g)	V_{meso} (cm^3/g)	V_t(cm^3/g)
CNTn	-	300	0.01	1.76	1.77
CNTb	-	264	0.09	0.62	0.71
AC	-	1487	0.52	0.62	1.14
CNTnCe20	19	207	0.07	0.78	0.85
CNTbCe20	19	201	0.07	0.50	0.57
CNTbCe40	37	203	0.07	0.45	0.52
CNTboxCe20	21	179	0.06	0.56	0.62
ACCe20	19	1083	0.37	0.47	0.84
CeO_2	-	101	0.04	0.07	0.11

[1]Determined by thermogravimetry.

The different morphology of CNTn and CNTb supports was confirmed by microscopy (Fig.SI 1). It can be seen that the CNTn support displayed larger straight graphitic planes, whereas the CNTb support presented more amorphous carbon and defects on the surface. Similar differences between both commercial CNT have already been reported in the literature [13]. The higher amount of amorphous carbon was also confirmed by the lower thermal stability observed in thermogravimetry (Fig.SI 2). The Raman spectra of CNTb and CNTn supports (Fig.SI 3) displayed the characteristics G (1595 cm^{-1}) and D (1315 cm^{-1}) bands ascribed to the in-plane vibrations of the C–C and to defective graphitic structures respectively. The I_D/I_G ratio estimated from the deconvolution of the

spectra was 1.81 for CNTn and 1.99 for CNTb. The lower ratio for CNTn indicates a more graphitic character for this sample, in agreement with the themogravimetry and the TEM results.

The differences in the ceria distribution on the supports can be observed on the TEM images shown in Fig. 2. The micrographs of support CNTnCe20 showed that ceria formed agglomerates of different sizes; however, ceria is more uniformly distributed as patches around the nanotubes or small particles on the external surface on the CNTbCe20 support. Regarding the CNTbCe40 sample, though some patches can be found on the micrographs, bigger agglomerates could also be observed. For the previously oxidized support, CNTboxCe20, ceria particles seemed to be well dispersed on the surface as very small particles, contrary to the other samples. In some areas where the nanotubes are open, as those shown in Fig. 2d, ceria nanoparticles might even be located inside the nanotubes. Concerning the sample ACCe20, a quite homogeneous dispersion of ceria on the surface was observed, without large agglomerates.

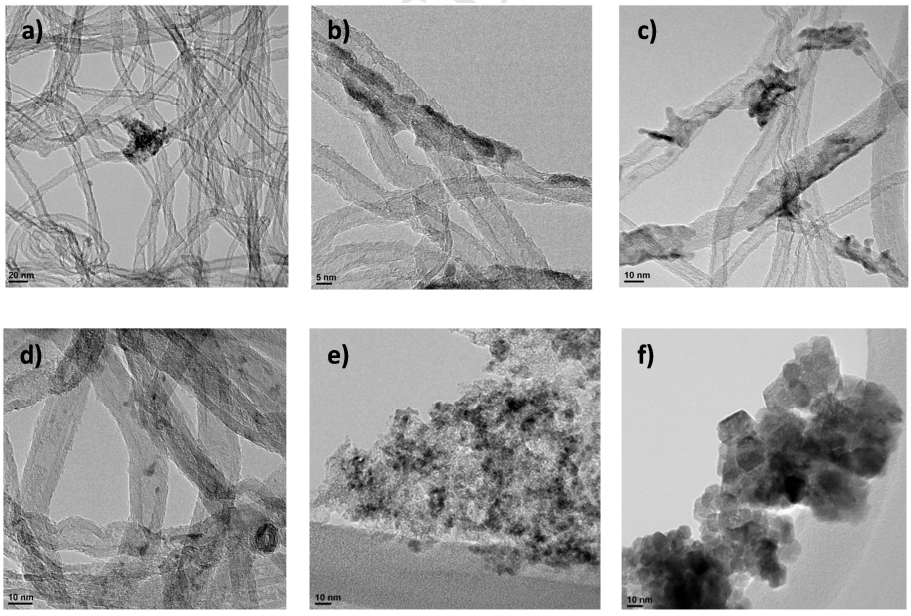

Figure 2. TEM micrographs of a) CNTnCe20, b) CNTbCe20, c) CNTbCe40, d) CNTboxCe20, e) ACCe20 and f) CeO_2.

The N_2 adsorption-desorption isotherms at 77 K for the ceria-CNT samples are shown in Fig.1b. The S_{BET} and pore volume values were estimated from these isotherms, and are shown in Table 1. The surface area and pore volume decreased upon ceria addition, this effect being more pronounced for the CNTnCe20 support. Two effects have to be considered when ceria is present. On one hand, ceria may block the pores of the support and, on the other hand, the addition of an oxide with a much lower surface area would reduce the surface per mass of material. Considering that most of the mesoporosity of the CNT support results from the free space created by the tubes, and that the ceria percentage was close to the nominal loading, the higher proportion of agglomerates observed for the CNTnCe20 support can explain the decrease of the S_{BET} value. In this sense, a higher decrease could be anticipated for CNTbCe40 compared to CNTbCe20. However, for the CNTb sample the amorphous carbon on the surface may contribute to the overall surface area and, in this case, the blockage of the pores would be more pronounced for CNTbCe20 support as a consequence of the ceria addition, as observed by TEM. With respect to CNTboxCe20 support, the oxidation treatment may have removed amorphous carbon to some extent and thus the S_{BET} decreased [14]. Finally, sample ACCe20 also showed lower S_{BET} and pore volume compared to AC due to the incorporation of ceria.

3.2 Catalysts characterization

TEM images of the fresh reduced catalysts are shown in Fig. 3. For the Ni/CNT samples, Fig. 3a and 3c, round-shaped Ni/NiO nanoparticles can be observed on the surface with an estimated average particle size of 4 and 5 nm for Ni/CNTn and Ni/CNTb catalysts, respectively. In general, the nanoparticles were located on the external surface of the nanotubes, and only in a few areas of Ni/CNTb they could be located inside the tubes, but this represented a very low percentage. As long as the Ni/CeO_2-CNT catalysts is concerned, though it is not possible to properly distinguish between CeO_2 and Ni due to their similar electron density, some differences can be envisaged. For example, considering that samples CNTnCe20 and CNTboxCe20 displayed large agglomerates and small nanoparticles of CeO_2 respectively, it is plausible to assume that the dispersed nanoparticles observed on the Ni/CNTnCe20 catalyst and the large particles on Ni/CNTboxCe20 would correspond to Ni/NiO species. For these catalysts, the images seem to indicate a low interaction between Ni and ceria. On the other hand, both Ni/CNTbCe20 and Ni/CNTbCe40 catalysts, whose Ni-free counterparts showed that ceria was mainly wrapped around the nanotubes, do not display dispersed nanoparticles as observed for Ni/CNTnCe20, what suggest that it is possible that the Ni/NiO nanoparticles are located close to the ceria patches and thus, they can not be distinguished, with preferential location on the surface of the CeO_2 and not on the bare carbon. Indeed, small nanoparticles located on top of the patches are observed, which could correspond to Ni/NiO species. Finally on both Ni/AC and Ni/ACCe20 catalysts (Fig. 3g and 3h) the active phases are homogeneously dispersed on the carbon support, with no large agglomerations. The estimated particle size of the Ni/NiO nanoparticles in Ni/AC catalyst was 7 nm.

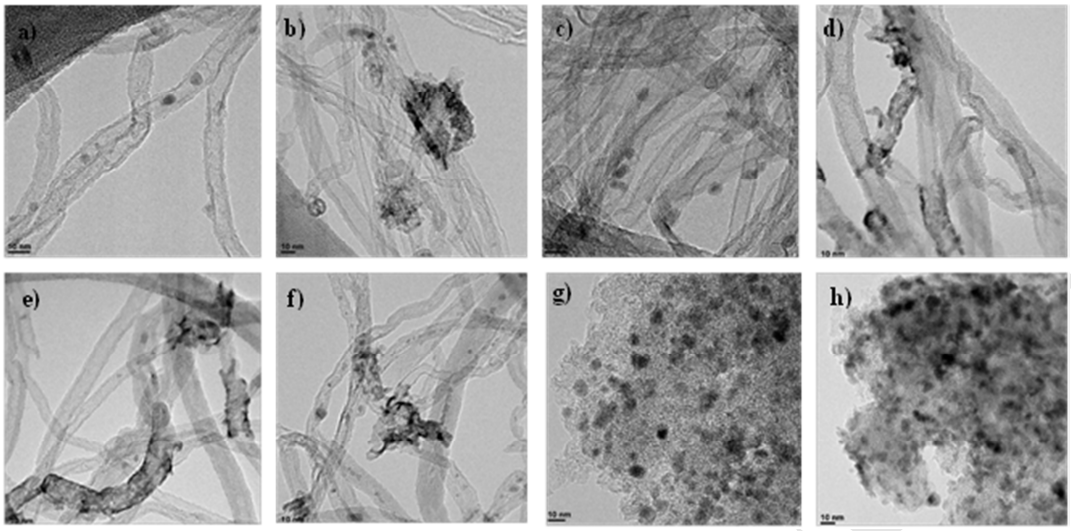

Figure 3. TEM micrographs of a) Ni/CNTn, b) Ni/CNTnCe20, c) Ni/CNTb, d) Ni/CNTbCe20, e) Ni/CNTbCe40, f) Ni/CNTboxCe20, g) Ni/AC and h) Ni/ACCe20.

The XRD patterns of the ceria containing catalysts are shown in Fig. 4. For the CNT based catalysts, besides the diffractions peaks at 26.1º and 43.1º corresponding to the (002) and (100) hkl reflections of graphite, the characteristic CeO_2 peaks at 28.6 º, 33.4º, 47.8 º and 56.7 º, corresponding to the diffractions in the (1 1 1), (2 0 0), (2 2 0) and (3 3 1) crystalline planes of the cubic fluorite type phase, can be clearly observed (JCPDS 34-0394). The intensity and wideness of the diffractions can be taken as an indication of the crystallinity.

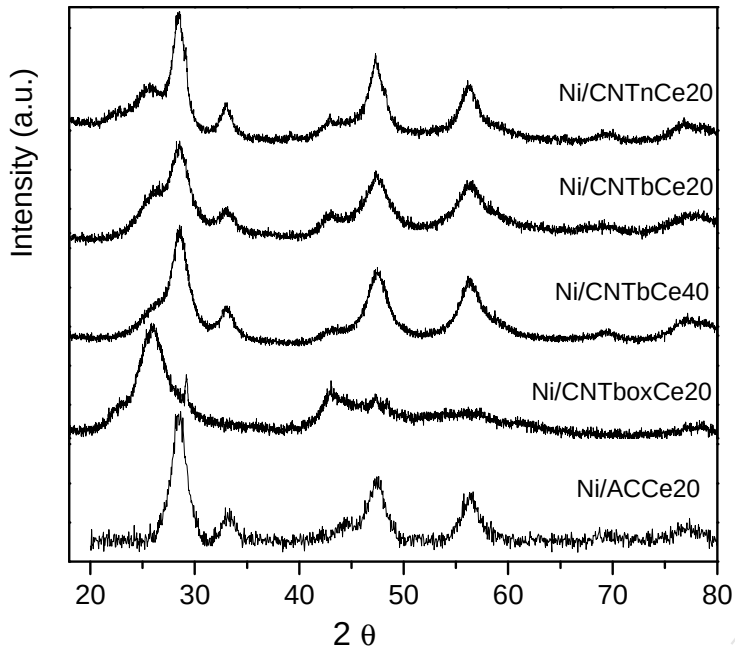

Figure 4. XRD profiles of the catalysts.

The XRD profile of the Ni/CNTnCe20 catalyst displayed the narrowest peaks among the samples, this indicating a high crystallinity. On the other hand, the Ni/CNTbCe40 catalyst showed more intense and sharp peaks compared to Ni/CNTbCe20, in agreement with the TEM analysis that showed larger particle size for the former. With respect to the oxidized sample, the diffraction peaks of ceria are only insinuated, and they seemed to overlap with those of graphite. This is consistent with the smaller crystal size of CeO_2 observed by TEM. For the Ni/ACCe20 catalyst only diffractions ascribed to ceria could be observed. The mean crystal sizes of CeO_2 were estimated by application of the Scherrer equation to the (1 1 1) diffraction peak, and they followed the order CNTbCe20 (3.5 nm) < CNTbCe40 (4.6 nm) ≈ ACCe20 (4.7 nm) < CNTnCe20 (5.3 nm) as the pattern observation suggested. The larger particle size upon increasing ceria loading was already reported for a Pt/AC system, where a 20 wt.% ceria content displayed smaller size than the samples with 30 and 40 wt.% loading [7]. It is likely that

at higher precursor concentration the diffusion of the resulting solution is hindered and ceria particles tend to agglomerate. In addition, the main diffraction peak at 2θ = 43.3, corresponding to the (200) plane of the NiO fcc phase, is observed in all samples in agreement with JCPDS no. 04-0835. This peak is smaller and much wider, indicating a small crystal size and a good dispersion (as it was also observed in TEM micrographs).

Fig. 5a shows the evolution of the H_2 consumption as a function of temperature for the ceria-carbon samples in H_2-TPR experiments. Bulk ceria displayed two reduction peaks at 773 and 1123 K, which corresponded to the reduction of surface and bulk ceria, respectively [15,16,5]. When ceria was supported on the carbon materials the reduction profiles were shifted to lower temperatures. The lower reduction temperature can be related to a better dispersion of ceria, as small ceria particles would lead to a larger proportion of surface ceria and easier reducibility of the bulk ceria, which is in agreement with the TEM and XRD results. For CNTboxCe20 and ACCe20 supports, the low temperature peak appeared at higher temperatures than for the other samples, what can be due to the additional contribution of the reduction of oxygen groups on the surface, or to the stronger interaction between the ceria precursor and the oxygen groups [17,18].

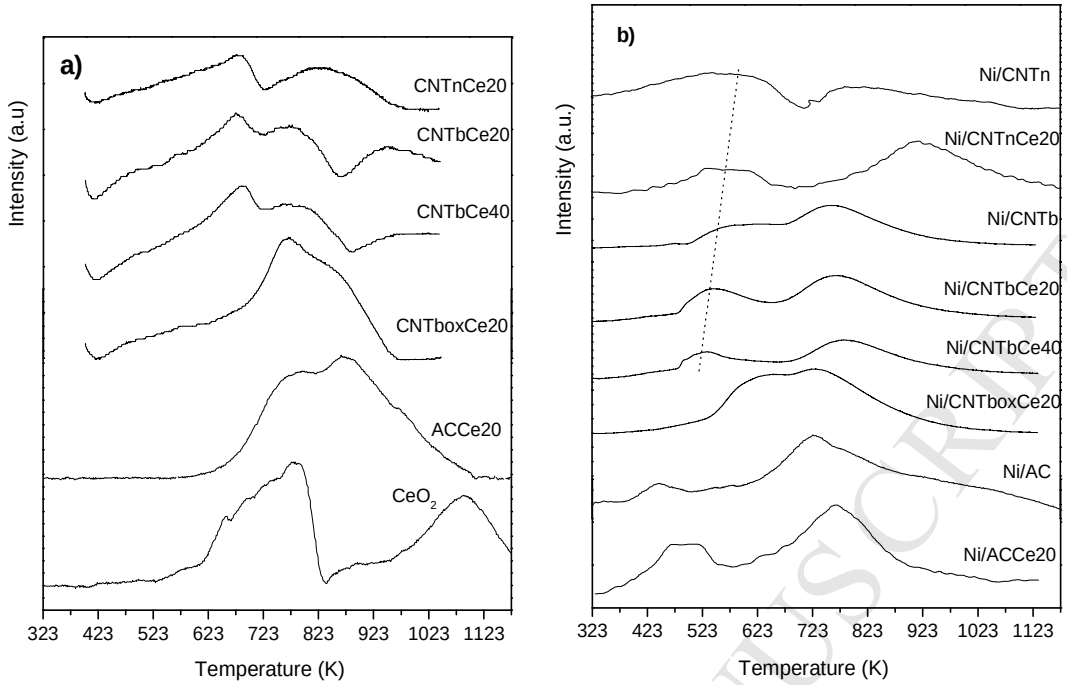

Figure 5. H_2-TPR profiles of the supports and catalyst.

The H_2-TPR profiles of the catalysts are shown in Fig. 5b. In general, the profiles showed two main peaks of hydrogen consumption with maxima in the range 442-643 K and 720-915 K. In the first peak, the consumption of hydrogen was observed along with the evolution of m/z = 18 as the main mass, and it can be observed that it is shifted to lower temperatures upon increasing the ceria content, except for the Ni/ACCe20 and Ni/CNTboxCe20 catalysts. The second reduction peak appeared along with m/z = 16 as the majority mass, together with m/z = 18 and m/z = 28, and it is shifted to higher temperatures upon increasing the ceria content except for Ni/CNTboxCe20. According to literature reports, the reduction of bulk NiO has been observed at around 638 K [19, 20]. When it is supported, the reducibility depends on the support, surface chemistry, metallic precursor and calcination temperature which further determinate the size, location and interaction with the support. Different TPR profiles have been

reported for nickel supported on carbon nanotubes depending on the surface chemistry, particle size and/or location of the particles [21,22]. The first reduction peak would correspond to the reduction of NiO, and the temperature at which it appears is in the range of previous reported values [23,24]. The shift to lower temperatures observed for the ceria containing samples would be due to the easier reducibility of NiO species in close contact with ceria. The observed exception displayed by the Ni/CNTboxCe20 catalyst can be ascribed to the strong interaction between Ni^{+2} and the remaining oxygen groups on the surface, as proposed in the literature [17,18]. On the other hand, several contributions might be included in the second reduction peak. The appearance of m/z = 16 indicates that at this temperature previously reduced nickel nanoparticles would act as catalyst for the methanation of the support, as previously reported [19,25]. The presence of m/z = 18 and m/z = 28 in this range of temperatures would result from the reduction of surface ceria and oxygen groups, respectively. This peak is slightly shifted to higher temperatures for Ni/CNTbCe20, Ni/CNTbCe40 and Ni/ACCe20 catalysts compared to their CeO_2-free counterpart, which might be due to the additional contribution of surface ceria reduction to the profile. The lower temperature at which this peak appeared for the catalyst Ni/CNTboxCe20 could be a consequence of the easier methanation of the open ends that this sample seemed to display, as the adsorption isotherm suggested. On the contrary, the more graphitic surface of the CNTn support may hinder the methanation, as this latter peak appeared at higher temperature for Ni/CNTnCe20 sample. For both Ni/CNTboxCe20 and Ni/CNTnCe20 catalysts, the H_2-TPR profiles seem to confirm the TEM observations that suggested low contact between Ni and ceria. The effect of ceria on the reducibility has been studied scarcely for other systems. For example for a Ni/SBA-15 catalyst a shift of 40 K to lower

reduction temperatures was found when 7.5 wt.% ceria was added, yielding Ni nanoparticles of 5 nm; however, bulk ceria was also present [26].

The most active catalyst and its counterpart without ceria, i.e. Ni/CNTbCe20 and Ni/CNTb, as well as the Ni/CeO_2 catalyst were studied by XPS after previous reduction at 623 K. The Ni $2p_{3/2}$ spectra of both CNT-based catalysts displayed several contributions, and the corresponding binding energies and the percentage of the different Ni species are reported in Table 2. The contribution at lower binding energy can be assigned to Ni^0; the two other contributions, at around 854.7 and 856.0 eV, are assigned to NiO and $Ni(OH)_2$ species, respectively [14,27]. The binding energies of these two Ni^{+2} species in the ceria-containing catalysts are slightly higher than the values reported for the pure compounds, and also than these species dispersed on the carbon-supported Ni/C catalyst, which is indicative of their interaction with ceria. This can be explained by a strong metal-support interaction between Ni and CeO_2 which can modify the electronic properties of Ni [33]. According to the results, none of the samples were completely reduced after the reduction treatment. Furthermore, the band corresponding to metallic Ni in the Ni/CeO_2 catalyst is strongly shifted to a higher binding energy, 853.5 eV, compared to the carbon-supported catalyst. These results confirm the existence of Ni-CeO_2 interactions, in agreement with the H_2-TPR profiles. The main line of Ce $3d_{5/2}$ core level appears at 882.1 eV for Ni/CeO_2 (not shown), and it is typically ascribed to CeO_2 species. The catalyst prepared over CNT, Ni/CNTbCe20, displayed the maximum at a slightly higher value, 882.6 eV, which might be due to the interactions between CeO_2 and nickel [28, 29].

Table 2. XPS data of Ni/CNTb, Ni/CNTbCe20 and Ni/CeO_2 reduced at 623 K.

Catalysts	Ni $2p_{3/2}$ (eV)		Ce $3d_{5/2}$ (eV)
	Ni^{2+}	Ni^0	
Ni/CNTb	854.7 (27)[1]	852.6 (33)	--
	856.0 (40)		
Ni/CNTbCe20	855.5 (40)	853.3 (20)	882.6
	857.7 (40)		
Ni/CeO_2	854.3 (42)	852.3 (19)	882.1
	856.4 (39)		

[1] Values in parenthesis indicate the percentage of Ni species from XPS areas

The characterization performed proved that a better Ni-ceria interaction was achieved on the CNTb-supported catalyst compared to CNTn, and that NiO particles were larger over CNTn than over CNTb. The better ceria dispersion over the support, as observed by XRD and TEM, favored the Ni-ceria interactions and, thereby the reduction process, as confirmed by H_2-TPR experiments.

3.3 Catalytic behavior

Fig. 6 displays the catalytic activity of the different samples in terms of CO conversion as a function of the reaction temperature. The CO conversion at each temperature has been determined after 1 h stabilization, and no deactivation was detected during this period. It has to be noted that all the catalysts were active, and the selectivity to CO_2 was 100% in the whole range of temperatures. The conversions obtained with the

Ni/CNTn and Ni/CNTnCe20 catalysts followed the same behavior, reaching a value of 41% at 533 K. It can be also observed that these catalysts showed the same tendency than Ni/CNTb. Catalysts prepared with CNTb as parent support were active at low temperatures, i.e. 433 K. However, while the conversion reached at 533 K for Ni/CNTbCe20 catalyst was 97%, the maximum conversion obtained for Ni/CNTbCe40, Ni/CNTboxCe20 and Ni/CNTb was 70%, 51% and 41%, respectively. On the other hand, the Ni/ACCe20 and Ni/AC catalysts achieved a maximum conversion of 97% and 64% respectively. In summary, the activity followed the trend: Ni/CNTbCe20 > Ni/CeO_2 > Ni/ACCe20 > Ni/CNTbCe40 > Ni/AC> > Ni/CNTboxCe20 > Ni/CNTb ≈ Ni/CNTn ≈ Ni/CNTnCe20. The results showed that Ni/CNTbCe20 displayed the highest activity among the catalysts, even better than the catalyst prepared over bulk ceria, Ni/CeO_2, and the analogous catalyst prepared over activated carbon. The catalytic activity was higher than that reported for a Ni (5%)/CeO_2 catalyst promoted with Re under similar reactions conditions (< 20% CO conversion rate at 533 K) [30].

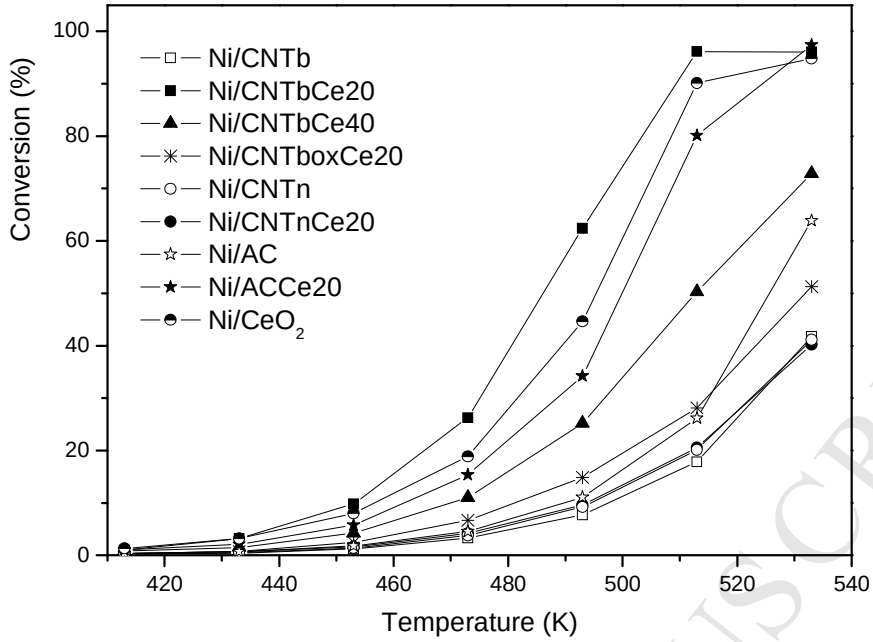

Figure 6. CO conversion *vs.* reaction temperature in idealized feed (1.87% CO, 35.92% H_2O, and He balance), for catalysts reduced at 623 K.

Two reaction mechanisms have been proposed for this reaction over ceria-based catalysts. The redox mechanism suggests that ceria redox process assists the oxidation of CO to CO_2 and the reduction of H_2O to H_2 [31]. The associative mechanism proposes that water is dissociated to hydroxyls on the vacancies of ceria, and they react with CO to yield formates and then CO_2 and H_2 [32]. Therefore, according to both mechanisms the presence of highly dispersed ceria, with a large available surface would improve the catalytic performance.

The catalytic activity yielded by catalyst Ni/CNTbCe20 is in agreement with the characterization results, which showed a better dispersion of ceria on this support and a better contact with the metallic phase. It is interesting to note that unlike to what was observed with platinum-based catalysts [7], nickel does not require the presence of ceria

to be active, as NiO is present in the catalyst at the reaction temperature. It has been suggested that the reaction mechanism over nickel is similar to that for copper, an associate mechanism similar to that proposed for ceria [11,33,34,10] in which water is dissociated on the partially oxidized Ni surface to produce adsorbed hydroxyl groups and atomic hydrogen. The hydroxyl groups would react with adsorbed carbon monoxide to form an intermediate, formate, which eventually decomposes into carbon dioxide and hydrogen.

Catalytic activity for the ceria-free Ni/CNTb, Ni/CNTn and Ni/AC catalysts was similar at low temperature, but then the Ni/AC catalyst achieved higher conversion upon increasing the temperature. The proposed mechanism over $Ni^{+\delta}$ is favored with small particle sizes. All the ceria-containing catalysts were more active than their ceria-free counterparts, except for Ni/CNTnCe20, what confirmed the important role of ceria on the catalytic performance when a good interaction between the metal and ceria is achieved.

The effect of ceria loading was studied by preparing a 40 wt.% loading catalyst over CNTb. This catalyst yielded lower activity compared with Ni/CNTbCe20, in line with the characterization results that showed larger ceria agglomerates in the Ni/CNTbCe40 catalyst.

With respect to Ni/CNTboxCe20, the reaction results are also in line with the characterization results that suggested a low amount of interacting Ni-CeO_2 species, despite the good dispersion of ceria revealed by TEM. It seems that the oxidation treatment changed the surface chemistry and opened the tips of the nanotubes to a certain extent. The ceria precursor would then be able to diffuse inside the tubes and CeO_2 nanoparticles were grown inside, hindering the access of nickel and therefore the Ni-ceria interaction.

The promotion effect of ceria has been studied over other nickel-supported systems. For example, the addition of different percentages of ceria to Ni-Al_2O_3 avoided nickel sintering and improved the catalytic performance in glycerol [16] and propane steam reforming [35]. The addition of ceria to Ni/SBA-15 catalyst was also found to be beneficial for the synthesis of 1,2-propanediol from glycerol, as a result of the different acidity [30].

In this study, a clear effect of the support on the ceria dispersion has been determined. The different morphology and surface chemistry of the support also influenced the catalytic behavior. In this sense, the similar activity of Ni/CNTn and NiCNTnCe20 catalysts is consistent with the characterization results. For the CNTn support, which showed a more graphitic surface, the dispersion of ceria was hindered and thereby the interaction between ceria and nickel species was very low. Moreover, the surface area decreased in a larger extent upon depositing ceria for Ni/CNTnCe20 compared to Ni/CNTbCe20. Considering the activity of ceria in the WGS reaction, an improvement on the activity was expected with catalyst Ni/CNTnCe20; however, the reduction of the surface area may have masked the increase of activity expected by ceria addition. The improvement of the catalytic performance over CNT supports has also been observed by comparing Ni/CNTbCe20 and Ni/ACCe20 catalysts. Despite the much higher surface area of activated carbon, which should result in a better dispersion, Ni/CNTbCe20 was more active than Ni/ACCe20. Furthermore, the improvement obtained by ceria addition was more pronounced for CNTb than for the AC supports, as the H_2-TPR results anticipated. It is well known that CNT supports can offer improved catalytic performance compared to AC for liquid phase reactions [36,37] and this effect has also been observed for certain gas phase reactions [8]. It has been suggested, for example, that the higher activity of Pt/CNT is due to the different dynamic of the reactants and

products on the closed nanotube surface compared to an open graphitic surface [38]. Furthermore, two characteristics may be responsible for this improvement when using CNT supports. The shape of the carbon nanotubes may promote the dispersion of ceria as thin layers around the tubes in a similar way as it was found for metal nanoparticles [39]. Additionally, the mesoporosity of the nanotubes could favor the access of the precursor solution to the entire surface, reaching a larger proportion of support area. Indeed, as the adsorption isotherms showed, a certain proportion of ceria might have been deposited inside the micropores of activated carbon, which would hinder the accessibility of reactants and products. Therefore, the surface of the CNT support in the Ni/CNTbCe20 catalyst is covered by ceria to a larger extent than the carbon surface in Ni/ACCe20, in which more bare support is present. Thus, nickel particles deposited on the bare carbon support are not able to interact with ceria, and this negatively affects the catalytic performance.

The most active catalyst, Ni/CNTbCe20, was also tested under more realistic conditions. Results of CO conversion are shown in Fig.7. We first studied the effect of increasing the CO concentration in the feed, and it can be seen that it decreased the catalytic activity (Fig. 7, Feed B). While under the ideal feed, Feed A, the temperature needed to achieve nearly full conversion was 513 K, when Feed B was employed the same conversion was achieved at 573 K. Nonetheless, the selectivity was 100 % to CO_2 under both feeds in the whole range of temperature.

The catalyst was also evaluated under a surrogate post reforming stream Feed C, with the aim to test its viability for a real application, for instance the use of a WGS reactor in an integrated fuel processor for pure hydrogen production. It can be observed that the CO conversion was slightly shifted to higher temperatures compared to Feed B, and the maximum conversion achieved under these conditions, 72%, was somewhat lower than

that corresponding to the equilibrium conversion, 82%. Furthermore, by using Feed C methane formation was observed although only at temperatures above 573 K, and it was mainly due to CO_2 hydrogenation, as no methane was observed when the CO_2-free feed stream was used, together with the presence of a high concentration of H_2 [27]. The lower catalytic activity under these conditions can be due to the larger amount of CO in the feed stream although, additionally, and according to literature, both CO_2 and H_2 can also have a negative effect in the WGS reaction rate [40]. While CO_2 may produce carbonates on the ceria surface [41, 42], an excess of hydrogen may lead to the irreversible over-reduction of ceria [43]. It is reported that bulk Ni species promote the formation of CH_4 under these WGS reaction conditions, and that metallic nickel is a well-known catalyst for methanation but, on the other hand, Ni-based catalysts are among the most effective and affordable metal catalysts for WGS [11, 44]. Another important issue that has been extensively studied is the nature of catalytically active species in the methanation process. It is well known that the hydrogenation process only takes place on metallic Ni^0 sites, and that other Ni species as oxides, hydroxides or carbides are not active in the methanation reaction.

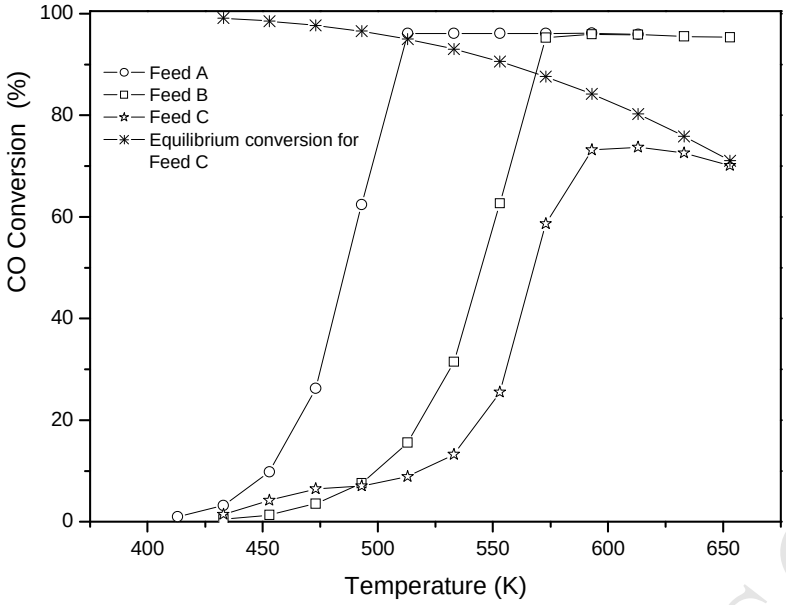

Figure 7. CO conversion *vs* reaction temperature in Feed A (1.87% CO, 35.92% H_2O, and He balance), Feed B (5% CO, 30% H_2O, and He balance) and Feed C (7% CO, 30% H_2O, 50% H_2, 9% CO_2 and He balance) for Ni/CNTbCe20 reduced at 623 K.

Finally, and with the aim of stress the much better performance of the Ni/CNTbCe20 catalyst in comparison with its counterparts, the catalytic behaviour of samples Ni/ACCe20 and Ni/CeO_2 was also studied under feeds B and C. The CO conversion vs. reaction temperature curves are presented in the Supplementary Information (Fig. S.I. 4 and Fig. S.I. 5). It can be seen that catalysts supported on activated carbon and bulk ceria are less active, especially at high temperatures. This is a proof of the advantages of using the CNTb as support for nickel and ceria in catalysts for the low temperature water-gas shift reaction.

4. Conclusions

Highly active Ni-Ce carbon nanotubes-supported catalysts (Ni/CeO_2/CNT) have been developed and tested in the low-temperature water-gas shift reaction. Cerium oxide (20

wt.%) has been dispersed over two commercial carbon nanotubes, and the results indicate that the morphology and the surface chemistry of the supports play an important role on the dispersion of ceria. XRD and TEM studies have confirmed the small crystal size (3-5 nm) and high dispersion of CeO_2 in comparison with massive CeO_2 catalysts (15 nm). Comparing the two commercial carbon nanotubes, those with less graphitic character afforded better ceria dispersion and better Ni-ceria interaction, this leading to a better catalytic performance. The effect of the surface oxidation of carbon nanotubes has been also studied, and it has been found that this treatment might open the nanotubes and favor the incorporation of ceria in the inner space, this hindering the Ni-ceria interaction which in turn resulted in worse catalytic performance. Increasing the ceria loading to 40 wt.% resulted in larger ceria agglomerates and, therefore, the catalytic activity was lower. The results obtained with the best catalyst based on carbon nanotubes were compared to those with an analogous catalyst prepared over activated carbon, and it was observed that the activity over the former was better, and this can be attributed to the better dispersion of ceria over the carbon nanotubes, despite their lower surface area, which favored a superior Ni-ceria interaction. In this way, the activity achieved over the best catalyst based on carbon nanotubes was better than over an analogous catalyst prepared over activated carbon, and even better than for the catalyst prepared over massive ceria, Ni/CeO_2. Moreover, catalysts without ceria were also active due to the presence of NiO species.

Finally, the catalyst that offered the highest activity under the ideal feed was evaluated under more realistic conditions to study the effect of the presence of CO_2 and H_2 in the feed. It has been found that the activity slightly diminished, and methane formation was only observed at temperatures higher than 573 K due to CO_2 hydrogenation.

The presented results show an interesting alternative catalyst for the low-temperature water-gas shift reaction, as better catalytic performances were obtained employing a much lower amount of ceria by increasing its available surface area.

Acknowledgements

Financial support from CONICYT (Chile, Postdoc FONDECYT 3130483), Ministerio de Economía y Competitividad (Spain, MAT2010-21147 and MAT2013-45008-P) and Generalitat Valenciana (Spain, PROMETEOII/2014/004) is gratefully acknowledged.

5. References

[1] Peña, M.A., Gómez, J.P., Fierro, J.L.G. New catalytic routes for syngas and hydrogen production. Appl Catal A 1996;144:7-57.

[2] Franchini, C.A., Duarte de Farias, A.M., Albuquerque, E.M., dos Santos, R., Fraga, M.A. Single-stage medium temperature water-gas shift reaction over Pt/ZrO_2 – Support structural polymorphism and catalyst deactivation. Appl Catal B 2012;117-118:302-309.

[3] Hinrichsen, K.O., Kochloefl, K., Muhler, M. Water gas shift and COS removal, in Handbook of Heterogeneous Catalysis, Wiley, 2008, vol. 8, pp. 2905-2920.

[4] Goscianskaa, J., Zioleka, M., Gibson, E., Daturi, M. Novel mesoporous zirconia-based catalysts for WGS reaction. Appl Catal B 2010;97:49-56.

[5] Iriondo, A., Barrio, V.L., Cambra, J.F., Arias, P.L., Guemez, M.B., Sanchez-Sanchez, M.C., Navarro, R.M., Fierro, J.L.G. Glycerol steam reforming over Ni catalysts supported on ceria and ceria-promoted alumina. Int J Hydrogen Energy 2010;35:11622 – 11633.

[6] Zhu, H., Wang, W., Ran, R., Shao, Z. A new nickel–ceria composite for direct-methane solid oxide fuel cells. Int J Hydrogen Energy 2013;38: 3741-3749.

[7] Buitrago, R., Ruiz, J., Silvestre-Albero, J., Sepúlveda-Escribano, A., Rodríguez-Reinoso, F., Water-gas shift reaction on carbon-supported Pt catalysts promoted by CeO_2. Catal Today 2012;180:19-24.

[8] Jardim, E., Gonçalves, M., Rico-Francés, S., Sepúlveda-Escribano, A., Silvestre-Albero, J. Superior performance of multi-wall carbon nanotubes as support of Pt-based catalysts for the preferential CO oxidation: Effect of ceria addition. Appl Catal B 2012;113:72-78.

[9]Hwang, K.R., Lee, C.B., Park, J.S. Advanced nickel metal catalyst for water–gas shift reaction. J Power Sources 2011;196:1349–1352.

[10] Li, Y., Fu, Q., Flitzani-Stephanopoulos, M. Low-temperature water-gas shift reaction over Cu- and Ni-loaded cerium oxide catalysts. Appl Catal B 2000;27:179–191.

[11] Kim, S.H. Nam, S.W., Lee, H.I. Effect of pretreatment on the activity of Ni catalyst for CO removal reaction by water–gas shift and methanation. Appl Catal B 2008;81: 97–104.

[12] Hong, Y.Q., Xiang, H.P., Shuo, B., Mao-Zhang, W., Hui-Ming, C. Adsorption and capillarity of nitrogen in aggregated multi-walled carbon nanotubes. J Chem Phys Lett 2001;345:18–24.

[13] Tessonnier, J.P., Rosenthal, D., Hansen, T.W., Hess, C., Schuster, M.E., Blume R. et al. Analysis of the structure and chemical properties of some commercial carbon nanostructures. Carbon 2009;47:1779–1798.

[14] Solhy, A., Machado, B.F., Beausoleil, J., Kihn, Y., Goncalves, F., Pereira, M.F.R., Orfao, J.J.M., Figueiredo, J.L., Faria, J.L., Serp, P. MWCNT activation and its influence

on the catalytic performance of Pt/MWCNT catalysts for selective hydrogenation. Carbon 2008;46:1194 –1207.

[15] Shinde, V.M., Madras, G., Nanostructured Pd modified Ni/CeO_2 catalyst for water gas shift and catalytic hydrogen combustion reaction. Appl Catal B 2013;132-133:28-38.

[16] Kugai, J., Miller, J.T., Guo, N., Song, C., Role of metal components in Pd–Cu bimetallic catalysts supported on CeO_2 for the oxygen-enhanced water gas shift. Appl Catal B 2011;105:306-316.

[17] Ebbsen, T. W., Hiura, H., Bisher, M.E., Treacy, M. M. J., Shreeve-Keyer, J. L., Haushalter, R. Decoration of carbon nanotubes. Adv Mater 1996;8:155-157.

[18]He, B., Wang, M., Sun, W., Shen, Z., Preparation and magnetic property of the MWNT-Fe^{2+} composite. Mater Chem Phys 2006;95:289-293.

[19]Ma, Q., Wang, D., Wu, M., Zhao, T., Yoneyama, Y., Tsubaki, N., Effect of catalytic site position: Nickel nanocatalyst selectively loaded inside or outside carbon nanotubes for methane dry reforming. Fuel 2013;108:430–438.

[20] Buitrago-Sierra, R., Ruiz-Martínez, J., Serrano-Ruiz, J.C., Rodríguez-Reinoso, F., Sepúlveda-Escribano, A. Ethanol steam reforming on Ni/Al_2O_3 catalysts: Effect of the addition of Zn and Pt. J Coll Interf Sci 2012;383:148–154.

[21] Lu, S., Zhang, C., Liu, Y., Carbon nanotube supported Pt–Ni catalysts for preferential oxidation of CO in hydrogen-rich gases. Int J Hydrogen Energy 2011;36:1939 - 948.

[22] Yang, H., Song, S., Rao, R., Wang, X., Yu, Q., Zhang, A. Enhanced catalytic activity of benzene hydrogenation over nickel confined in carbon nanotubes. J Mol Catal A 2010;323:33–39.

[23] Liu, H., Wang, H., Shen, J., Sun, Y., Liu, Z. Promotion effect of cerium and lanthanum oxides on Ni/SBA-15 catalyst for ammonia decomposition. Catal Today 2008;131:444–449.

[24] Burattin, P., Che, M., Louis, C. Ni/SiO_2 Materials Prepared by Deposition−Precipitation: Influence of the Reduction Conditions and Mechanism of Formation of Metal Particles. J Phys Chem B 2000;104:10482-10489.

[25] Nieto-Márquez, A., Gil, S., Romero, A., Valverde, J.L., Gómez-Quero, S., Keane, M.A. Gas phase hydrogenation of nitrobenzene over acid treated structured and amorphous carbon supported Ni catalysts. Appl Catal A 2009;363:188–198.

[26] Jiménez-Morales, I., Vila, F., Mariscal, R., Jiménez-López, A. Hydrogenolysis of glycerol to obtain 1,2-propanediol on Ce-promoted Ni/SBA-15 catalysts. App Catal B 2012;117– 118:253– 259.

[27] Czekaj, I., Loviat, F., Raimondi, F., Wambach, J., Biollaz, S., Wokaun, A. Characterization of surface processes at the Ni-based catalyst during the methanation of biomass-derived synthesis gas: X-ray photoelectron spectroscopy (XPS). Appl Catal A 2007;329:68-78.

[28] Van Ryneveld, E., Mahomed, A.S., Van Heerden, P.S., Green, M.J., Friedrich, H.B. A catalytic route to lower alcohols from glycerol using Ni-supported catalysts. Green Chem 2011;13:1819-1827.

[29] Senanayake, S.D., Rodriguez, J.A., Stacchiola, D. Interactions of Ni Nanoparticles with Reducible CeO_2(111) Thin Films. J Phys Chem C 2012;116:9544-9549.

[30] Chayakul, K., Srithanratana, T., Hengrasmee, S., Catalytic activities of Re–Ni/CeO_2 bimetallic catalysts for water gas shift reaction. Catal Today 2011;175:420–429.

[31] Shido, T., Iwasawa, Y. Reactant-promoted reaction mechanism for Water-Gas Shift reaction on Rh-doped CeO_2. J Catal 1993;141:71–81.

[32] Andreeva, D., Idakiev, V., Tabakova, T., Andreev, A., Giovanoli, R. Low-temperature Water–Gas Shift Reaction over Au/α-Fe_2O_3. J Catal 1996;158:354–355.

[33] Spencer, M.S. The role of adsorbed oxygen as a promoter in reactions over industrial catalysts. Catal Today 1992;12:453-464.

[34] Chinchen, G.C., Spencer, M.S. A comparison of the water-gas shift reaction on chromia-promoted magnetite and on supported copper catalysts. J Catal 1988;112:325-327.

[35] Natesakhawat, S., Oktar, O., Ozakan, U.S. Effect of lanthanide promotion on catalytic performance of sol–gel Ni/Al_2O_3 catalysts in steam reforming of propane. J Mol Catal A 2005;241:133-146.

[36] Serp, P., Corrias, M., Kalck, P. Carbon nanotubes and nanofibers in catalysis, Appl Catal A 2003;253:337–358.

[37] Zhu, J., Holmen, A., Chen, D. Carbon Nanomaterials in Catalysis: Proton Affinity, Chemical and Electronic Properties, and their Catalytic Consequences. ChemCatChem 2013;5:378-401.

[38] Tanaka, K., Shou, M., Zhang, H., Yuan, Y., Hagiwara, T., Fukuoka, A., Nakamura, J., Lu, D. An Extremely Active Pt/Carbon Nano-Tube Catalyst for Selective Oxidation of CO in H_2 at Room Temperature. Catal Lett 2008;126:89–95.

[39] Nhut, J.M., Pesant, L., Tessonnier, J.P., Winé, G., Guille, J., Pham-Huu, C., Ledoux, M.J., Mesoporous carbon nanotubes for use as support in catalysis and as nanosized reactors for one-dimensional inorganic material synthesis. Appl Catal A 2003;254:345–363.

[40]Lin, J-H., Guliants, V.V. Hydrogen Production through Water–Gas Shift Reaction over Supported Cu, Ni, and CuNi Nanoparticle Catalysts Prepared from Metal Colloids. ChemCatChem 2012;4:1611-1621.

[41] Kim, C.H., Thompson, L.T. Deactivation of Au/CeOx water gas shift catalysts. J Catal 2005;230:66-74.

[42] Liu, X., Ruettinger, W., Xu, X., Ferrauto, R. Deactivation of Pt/CeO_2 water-gas shift catalysts due to shutdown/startup modes for fuel cell applications. Appl Catal B 2005;56:69-75.

[43] Zale, J.M., Sokolovskii, V., Löffer, D.G. Are noble metal-based water–gas shift catalysts practical for automotive fuel processing?. J Catal 2002;206:169-171.